Physics of Fluids

Large eddy simulations of solitons colliding with intrusions

Cite as: Phys. Fluids **32**, 096606 (2020); https://doi.org/10.1063/5.0021196
Submitted: 08 July 2020 • Accepted: 08 September 2020 • Published Online: 25 September 2020

Luisa Ottolenghi, Claudia Adduce, Federico Roman, et al.

View Online Export Citation CrossMark

ARTICLES YOU MAY BE INTERESTED IN

Intrusions and solitons: Propagation and collision dynamics
Physics of Fluids **32**, 076605 (2020); https://doi.org/10.1063/5.0011604

How does three-dimensional canopy geometry affect the front propagation of a gravity current?
Physics of Fluids **32**, 096605 (2020); https://doi.org/10.1063/5.0019760

Interfacial solitons propagating through a background shear current
Physics of Fluids **32**, 106603 (2020); https://doi.org/10.1063/5.0023567

APL Machine Learning
Open, quality research for the networking communities
Now Open for Submissions
LEARN MORE

AIP Publishing

© 2020 Author(s).

Physics of Fluids ARTICLE scitation.org/journal/phf

Large eddy simulations of solitons colliding with intrusions

Cite as: Phys. Fluids 32, 096606 (2020); doi: 10.1063/5.0021196
Submitted: 8 July 2020 • Accepted: 8 September 2020 •
Published Online: 25 September 2020

View Online Export Citation CrossMark

Luisa Ottolenghi,[1] Claudia Adduce,[2] Federico Roman,[3] and Giovanni la Forgia[4,a)]

AFFILIATIONS

[1]High Council for Public Works, Ministry of Infrastructure and Transport, 00161 Rome, Italy
[2]Department of Engineering, Roma Tre University, 00146 Rome, Italy
[3]Iefluids, Piazzale Europa, 1, 34127 Trieste, Italy
[4]Institute of Marine Sciences, National Research Council, 00133 Rome, Italy

[a)]**Author to whom correspondence should be addressed:** giovanni.laforgia@uniroma3.it

ABSTRACT

The dynamics of lock-release Intrusive Gravity Currents (IGCs) generating Internal Solitary Waves (ISWs) are investigated by three-dimensional large eddy simulations. We set the numerical, laboratory-scale domain in order to release a uniform fluid in multi-layer, stratified ambient, exciting pycnocline displacements. By adopting different initial settings, we analyzed the influence of the ambient stratification on both IGCs and ISWs features. We present the main flow dynamics and the time evolution of IGC and ISW front and trough positions, respectively. During the simulations, the ISW is allowed to reach the vertical wall at the end of the domain, and it undergoes reflection. We then analyzed the interaction between the IGC and the reflected ISW: the wave is observed to accelerate as it is pushed upwards by the intrusion, which, in turns, flows below the ISW, decelerating. By analyzing instantaneous velocity fields and flow rates, we found that during this interaction, the ISW increases its celerity in response of the reduced area available for its propagation, partially occupied by the intrusion, and because the velocity field in the IGC interface surroundings acts to facilitate the ISW passage.

Published under license by AIP Publishing. https://doi.org/10.1063/5.0021196

I. INTRODUCTION

A gravity current is the flow of one fluid within another ambient fluid caused by horizontal density gradients. When the density of the current is higher or lower than that of the ambient, bottom or buoyant gravity currents develop, respectively. If the density of the ambient fluid varies along the depth and the current has an intermediate density, an Intrusive Gravity Current (IGC), or intrusion, develops. Oceans and atmosphere are frequently characterized by regions with sharp density gradients along the vertical direction, called thermocline and tropopause, respectively. In this context, if a fluid of an intermediate density is released, it spreads along the interface of the two-layer stratified ambient, mixing and diluting. Releases can be both natural (river plumes, oceanic currents, thunderstorm outflows, and sea breeze fronts) or man-made (oil spillages, pollutant releases, and dense industrial gas spreads). Consequently, the knowledge of intrusion dynamics and water properties is fundamental for environmental sciences and prevention from natural disasters.[1]

During their propagation, IGCs can interact with the ambient stratification, producing a vertical displacement of the fluid interface and giving rise to an Internal Solitary Wave (ISW). ISWs are thus generated in response to a perturbation of the stable stratification of the pycnocline.[2–4] The generation of ISWs caused by river plumes was observed in real cases by satellite images both in coastal oceans and lakes. Nash and Moum[5] presented measurements of velocity, density, and acoustic backscatter across the Columbia River plume front, demonstrating that this mechanism is able to generate ISWs with similar amplitudes and steepness as internal waves observed elsewhere for tidal and topography interaction.[3,6] Valerio *et al.*[2] and Vilhena, Marti, and Imberger[7] investigated the dynamics of internal waves in Lake Iseo (Italy), which is characterized by the presence of a large island, which causes wind generated ISWs packets to potentially break. The formation of ISWs by frontally forced intrusion was detected and recorded by echo-sounder, current and density measurements taken along two transects in the Saguenay Fjord, Canada.[8] Toberman *et al.*[9] recorded the Loch Etive tidal outflow,

into the Ardmucknish Bay (west coast of Scotland, UK), induced by both the density difference and barotropic pressure gradient driven by tidal displacements. They observed the outflow behaving like a gravity current, which generates ISWs. The latter, detaching from the head of the intrusion, rebound on the frontal headland and are partially reflected toward the source of the buoyancy input. Similar processes were previously observed also by Thorpe, Hall, and Hunt,[10] who described bouncing internal bores in the same region, and by Xie, Li, and Boicourt.[11] These phenomena, as assessed by Toberman *et al.*,[9] are likely to characterize many fjordic systems located in the Scotland western coast and throughout the world oceans.

To idealize the complex scenarios of the real-world geophysical flows described above, IGCs and ISWs have been the subject of many experimental and theoretical studies,[12,13] and the lock-exchange laboratory-scale setup is frequently adopted.[14–17] It allows to reproduce unsteady density flows and solitary waves by both laboratory experiments[18–21] and numerical simulations.[20,22–25] This method consists in dividing the domain in two different regions by a gate and filling them with fluids of different densities. At the removal of the gate, the fluid in the lock propagates in the ambient forming a gravity current or generating solitary waves, depending on both the lock configuration and the ambient stratification.

Numerous experiments on intrusions propagating in a linearly[12,26] or two-layer[27,28] stratified ambients have been performed since the last five decades. In most of these studies, the current was characterized by a density ρ_i equal to the average of the ambient density, and no deflections of the interface upon the evolution of the intrusion were observed. De Rooij, Linden, and Dalziel[29] performed experiments with equal layer depths, but the density of the intrusion was no longer the average of the layer densities, and they clearly identified large-amplitude ISW flowing ahead of the intrusion. The velocity structure of a double-symmetric IGC was investigated by Lowe, Linden, and Rottman[30] through shadowgraph and particle tracking methods. They divided the flow in three regions: an energy conserving front, followed by a dissipative wake region characterized by billows, and a tail region.

Lock-exchange intrusions were studied experimentally by Sutherland[31] and Mehta, Sutherland, and Kyba[32] by the generation of successive releases into an initially two-layer stratified ambient with an interface region, which gradually widens to become a three-layer ambient. In the study of Sutherland and Nault,[33] the influence of the thickness of the ambient interface was investigated for symmetric intrusions, observing that the intrusion significantly decelerates when the interface thickness widens. This has to be considered in real geophysical flows, where the interface thickness cannot always be neglected.

Symmetric and nonsymmetric intrusions were further investigated by Cheong, Kuenen, and Linden[34] through laboratory experiments and 2D numerical simulations. They provided a new description of the intrusion velocity based on the conversion of the available potential energy into kinetic energy: for IGC with density equal to the depth-weighted mean of the layer densities, the front speed is a minimum (flat interface ahead the current), and for nonsymmetric intrusions, the speed is a function of the layers densities and the ratio of the layer depths. Their results were confirmed by the analytical model of Flynn and Linden,[35] which also include the interface deflection of the ISW preceding the intrusion, inferring that the energy carried by the wave is small if compared with the IGC energy.

In the experimental study of la Forgia *et al.*,[36] lock-release nonsymmetric IGCs were generated in different ambient stratifications characterized by an intermediate layer thickness widening by the generation of successive releases into a initially two-layer stratified ambient. In their experiments, a sloping bottom was placed at different locations along the tank in order to cause the different breaking mechanisms of the ISW, depending on the inclination of the slope.[15] After the ISW reached the sloping boundary, part of the ISW was also reflected by the slope and interacted with the IGC. They found that the collision affects both IGC and ISW features, leading the first to decelerate and the waves to accelerate.

High-resolution numerical models that solve the Boussinesq form of the Navier–Stokes equations such as Direct Numerical Simulations (DNSs) and Large Eddy Simulations (LESs) have been used to study bottom propagating unsteady gravity currents in different configurations.[37–44] These models allow to gain three-dimensional information about the density and velocity fields of the flow, with a detail that is rarely possible to achieve during laboratory experiments. Although numerous two-dimensional DNSs and LESs have been developed to support experimental observation and theoretical models of intrusions flowing into a two-layer stratified ambient,[33,34,45,46] to the authors' knowledge, three-dimensional numerical studies have not been developed yet to study IGCs. In particular, for the first time, the interaction between an ISW and the IGC is investigated by LESs. The lock-exchange setup is reproduced numerically, and both the ambient stratification and the released volume's geometry are varied. Different intrusions and ISWs with varying features (amplitude, length and celerity) are generated and are allowed to flow for relatively long distances. Taking inspiration from the experiments performed by la Forgia *et al.*[36] where the ISW is allowed to interact with an upsloping bottom and, after breaking, it is partially reflected flowing to, and interacting with, the IGC, the simulations presented here are extended up to the times after the interaction of these two phenomena. Our aim is to deepen the knowledge of the flow dynamics in those ambients, such as fjords, closed basins, lochs, and lakes, in which the interaction of these two phenomena is observed to occur.[9,11] The three-dimensional highly resolved density and velocity fields produced by three-dimensional LESs, indeed, allow us to address several scientific questions:

1. How does the stratification of the ambient affect the IGC and the ISW characteristics?
2. How do the density and velocity patterns of an IGC affect the dynamics of an ISW?
3. How does the ISW interact with the IGC that had generated it?
4. How do these two phenomena behave during their collision?

The present paper is organized as follows. The problem formulation and the numerical model are presented in Sec. II; in Sec. III, results are reported and discussed; conclusions are given in Sec. IV.

Published under license by AIP Publishing

II. PROBLEM FORMULATION

A. Numerical model

The large eddy simulation approach is based on the direct resolution of the large scales of motion through the integration of the governing equations and on the modeling of the small and dissipative scales of turbulence as subgrid stresses (SGS).[47] Present LESs are performed by using the numerical model of Armenio and Sarkar,[48] widely validated and employed over the years.[22,42,43,49,50] Their numerical model is based on the filtered, Boussinesq approximated, Navier–Stokes equations (LES filtering operation is indicated with the symbol $\bar{\square}$),

$$\frac{\partial \bar{u}_j}{\partial x_j} = 0, \tag{1}$$

$$\frac{\partial \bar{u}_i}{\partial t} + \frac{\partial \bar{u}_j \bar{u}_i}{\partial x_j} = -\frac{1}{\rho_0}\frac{\partial \bar{p}}{\partial x_i} + \frac{\partial}{\partial x_j}\left(\nu \frac{\partial \bar{u}_i}{\partial x_j}\right) - \frac{\rho'}{\rho_0} g \delta_{i2} - \frac{\partial \tau_{ij}}{\partial x_j}, \tag{2}$$

$$\frac{\partial \bar{s}}{\partial t} + \frac{\partial \bar{u}_j \bar{s}}{\partial x_j} = \frac{\partial}{\partial x_j}\left(k_s \frac{\partial \bar{s}}{\partial x_j}\right) - \frac{\partial \lambda_j}{\partial x_j}, \tag{3}$$

where u_i are the velocity components u, v, and w along the x (streamwise direction), y (vertical direction), and z (spanwise direction) axes, respectively (Fig. 1). In Eq. (2), p denotes the hydrodynamic pressure, and in Eq. (3), s is the salinity; the gravitational acceleration acting along x_2 or y direction is g. The kinematic viscosity and the molecular salt diffusivity are represented by the terms ν and k_s in (2) and (3), respectively, while ρ' is the variation of density with respect to the reference value ρ_0 (corresponding to the reference salinity s_0). Due to the isothermal condition of the flow, the state equation can be written as follows:

$$\rho = \rho_0 \left[1 + \beta(s - s_0)\right], \tag{4}$$

where β is the salinity contraction coefficient. The SGS momentum and salinity fluxes are indicated by the terms τ_{ij} and λ_j in Eqs. (2) and (3), respectively, and are modeled using the dynamic Smagorinsky eddy viscosity model.

The Lagrangian approach of Meneveau, Lund, and Cabot[51] is applied for the estimation of the constants of the model needed for the resolution of the SGS viscosity and diffusivity fluxes. The governing equations are solved numerically using the semi-implicit fractional-step method of Zang, Street, and Koseff.[52] The time advancement of the advective terms is solved by applying the second-order Adams–Bashforth technique, while the diagonal diffusive terms are solved through the implicit Crank–Nicolson scheme. Spatial derivatives are discretized by a second-order centered scheme, and the pressure equation is solved by a multigrid SOR-algorithm. Further details about the model and the subgrid stress implementation are given in the work of Ottolenghi *et al.*,[43] Armenio and Sarkar, and[48] Armenio and Piomelli.[53]

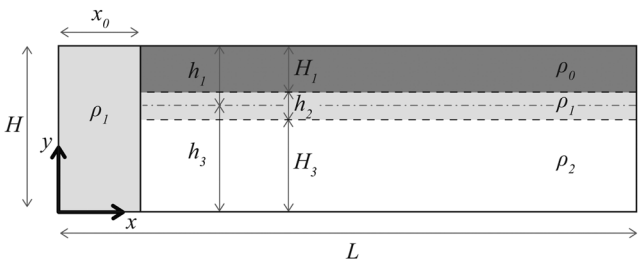

FIG. 1. Sketch of the lock-exchange configuration.

Flat, no-slip surfaces are set along the streamwise axis at $x = 0$ and $x = L$, where L is the total length of the domain. The vertical direction is characterized by the no-slip condition at $y = 0$, while the shear-free boundary condition is applied at the top boundary $y = H$, where H represents the domain's height (Fig. 1). Periodicity is employed in the z direction of the channel, characterized by a total width $W = H$. Zero flux of the scalar is imposed at all the boundaries.

A constant Courant number equal to 0.6 is used to set the time step of the simulations. The Schmidt number Sc, defined as the ratio between the kinematic viscosity and the molecular diffusivity, is fixed to 600, i.e., the reference value for salty water.

The flow field is initialized with the fluid at rest everywhere. A spatial distribution of the scalar is given at $t = 0$ in order to assure a density distribution coherent with the initial density distribution set for each run.

The overbar notation is herein omitted for simplicity although all the quantities refer to the LES-filtered results.

B. Numerical setup

To investigate the dynamics of ISWs generated by IGCs and their mutual interaction, we set the numerical domain with a lock-exchange configuration (Fig. 1).

The numerical domain is 2.16 m long, 0.2 m high, and 0.2 m wide, corresponding to $10.8H \times H \times H$ along the x, y, and z directions, respectively. Similar domain dimensions can be observed in some of the experimental cases shown in la Forgia *et al.*,[36] i.e., the ones characterized by the intermediate location of the sloping boundary. The streamwise direction is discretized by 1024 grid cells, resulting in a constant $\Delta x = 0.01H$; 64 cells are set for the spanwise direction ($\Delta z = 0.016H$); 256 cells span the vertical direction, with a non-uniform grid spacing, ranging between $0.01H$ (far from the pycnocline region) to $0.002H$ for the region characterized by sharp changes in density (pycnocline). For that region, 186 grid points are used in order to obtain detailed numerical results where the most significant dynamical processes are expected to develop.

The initial density field is imposed in order to reproduce the different runs performed. In particular, a vertical discontinuity is located at the distance x_0 from the left wall of the domain in order to set different density distributions within the lock and the ambient fluid regions. For our cases, the lock length x_0 ranges between 0.1 m and 0.05 m (i.e., $0.5H$–$0.25H$). The lock is composed by fluid of the density ρ_1, while the ambient fluid is characterized by a three-layer stratification. The lower layer has a density $\rho_2 > \rho_1$, the intermediate layer has a density equal to the lock one, ρ_1, and the upper layer has a density $\rho_0 < \rho_1$. We set a total water depth H = 0.2 m for the entire domain, and for each run, we vary the layers thickness composing the ambient fluid. In particular, the upper layer depth, h_1, assumes values of 0.03 m, 0.04 m, and 0.05 m

Published under license by AIP Publishing

(i.e., $0.15H$–$0.2H$–$0.25H$). The lower layer depth is $h_3 = H - h_1$. The middle layer is centered at the interface between the surrounding layers and has a thickness h_2 equal to 0.005 m, 0.015, m and 0.03 m, depending on the run (i.e., $0.025H$–$0.075H$–$0.15H$). Thus, the net depths of the upper and lower layers are $H_1 = h_1 - h_2/2$ and $H_3 = h_3 - h_2/2$, respectively (see Fig. 1). We remark that $h_2 = 0.005$ m represents, approximately, the minimal thickness of the pycnocline that can be reached for a two-layer stratified ambient in a laboratory experiment.[36] The initial buoyancy gradient driving the motion is varied for each run by fixing the lower layer density ρ_2 equal to 1030 kg/m^3 or 1040 kg/m^3 and the upper layer density ρ_0 to 1000 kg/m^3 or 1010 kg/m^3; the density in the lock ρ_1 is kept constant to 1020 kg/m^3 for all runs. Following Flynn and Linden,[35] different initial reduced gravities can be defined,

$$g'_{Li} = g\,\frac{\rho_2 - \rho_1}{\rho_{00}} \tag{5}$$

is the reduced gravity of the intrusion and the lower layer, with ρ_{00} being a characteristic density and g being the gravity acceleration,

$$g'_{Ui} = g\,\frac{\rho_1 - \rho_0}{\rho_{00}} \tag{6}$$

is the reduced gravity of the intrusion and the upper layer, and

$$g'_{LU} = g'_{Li} + g'_{Ui} = g\,\frac{\rho_2 - \rho_0}{\rho_{00}} \tag{7}$$

represents the reduced gravity of the interface.

The Reynolds number characterizing the flow can be defined as

$$\mathrm{Re} = \frac{u_b\,H}{\nu}, \tag{8}$$

where u_b is the buoyancy velocity, defined here with the maximum reduced gravity (i.e., g'_{LU}) as

$$u_b = \sqrt{g'_{LU}\,H}. \tag{9}$$

For the present simulations, Re = 56 029 or Re = 48 522 depending on the run.

Following Sutherland, Kyba, and Flynn,[54] two other important dimensionless parameters characterizing the flow can be defined,

$$\Delta = \frac{h_1 - h_3}{H}, \tag{10}$$

which represents the relative flow depths of the upper and lower layer ($\Delta = 0$ means that the intrusion is released in a symmetrical ambient, i.e., $h_1 = h_3$), and

$$\varepsilon = \frac{\rho_1 - \rho_{mean}}{\rho_2 - \rho_0}, \tag{11}$$

which measures the relative density difference between the intrusion and the upper- and lower-layer ambient ($\varepsilon = 0$ means that the density of the intrusion equals the depth-averaged densities of the ambient). Here, ρ_{mean} is the mean density of the ambient fluid,

$$\rho_{mean} = \frac{\rho_0\,H_1 + \rho_1\,h_2 + \rho_2\,H_3}{H}. \tag{12}$$

Totally, 14 LESs are performed by varying the ambient stratification (layers depths and densities) and the lock position (Table I).

TABLE I. Parameters of numerical simulations.

NAME	h_2 (m)	h_1 (m)	x_0 (m)	ρ_0 (kg/m^3)	ρ_2 (kg/m^3)
P1H1X1D0	0.005	0.030	0.100	1000	1040
P2H1X1D0	0.015	0.030	0.100	1000	1040
P3H1X1D0	0.030	0.030	0.100	1000	1040
P1H2X1D0	0.005	0.040	0.100	1000	1040
P1H3X1D0	0.005	0.050	0.100	1000	1040
P1H1X2D0	0.005	0.030	0.050	1000	1040
P1H1X1D1	0.005	0.030	0.100	1000	1030
P2H1X1D1	0.015	0.030	0.100	1000	1030
P3H1X1D1	0.030	0.030	0.100	1000	1030
P1H2X1D1	0.005	0.040	0.100	1000	1030
P1H3X1D1	0.005	0.050	0.100	1000	1030
P1H1X2D1	0.005	0.030	0.050	1000	1030
P1H1X1D2	0.005	0.030	0.100	1010	1040
P1H3X1D2	0.005	0.050	0.100	1010	1040

The reference case is P1H1X1D0, and parameters are varied for comparison with it. We identify each run by a notation described herein: P is for the pycnocline thickness, h_2, which assumes three different values (P1, P2, and P3); H is for the thickness of the upper layer, h_1, which also adopts three different values (H1, H2, and H3); X is for the lock position, x_0, placed at two different streamwise locations (X1, X2); D is for the densities of the upper and lower layers, varying in three different configurations (D0, D1, and D2).

III. RESULTS AND DISCUSSION

A. Flow features

The simulation begins by allowing the fluid into the lock to interact with the ambient: an IGC develops and propagates downstream intruding the pycnocline. At a later stage, an ISW forms nearby the nose of the current and gradually detaches from the intrusion due to its higher celerity. Once the ISW reaches the end of the domain, it is reflected by the right-wall, flowing backward to the source of buoyancy. As the reflected ISW reaches the same streamwise location of the IGC, they interact. During their collision, the wave is compressed in the upper layer losing its original shape, while the intrusion is pushed, in turns, at lower depths. As the head region of the intrusion overtakes the wave trough, the two phenomena can be distinguished again: the current loses energy and decelerates, while the wave continues flowing leftward.

To accurately analyze the flow dynamics, we study the evolution of the dimensionless density field ρ^*, defined as

$$\rho^*(x,y,z,t) = \frac{\rho(x,y,z,t) - \rho_0}{\rho_2 - \rho_0}. \tag{13}$$

Since the buoyancy force driving the motion predominantly acts along the x–y plane, the main flow features can be correctly captured by averaging the characteristic variables along the spanwise direction of homogeneity, and the flow can be described as essentially two-dimensional. However, we highlight that turbulent secondary

Published under license by AIP Publishing

effects on the flow dynamics, acting along the spanwise direction, are already taken into account due to the three-dimensionality of the present LESs: 3D patterns are allowed to develop, and isotropic dissipation effects can correctly occur and eventually affect the main flow evolution.

We evaluate the spanwise-averaged density field of the flow, $\langle\rho^*\rangle$, for the reference run (P1H1X1D0) at different dimensionless times $T^* = (tu_b)/x_0$, in order to present the main dynamics of the flow (Fig. 2). We use $x^* = x/x_0$ and $y^* = y/H$ as dimensionless length scales for the x and y axes, respectively. The interface between the IGC and the ambient region, as well as the pycnocline region, is identified by the isodensity levels $\langle\rho^*\rangle = 0.1$ and $\langle\rho^*\rangle = 0.9$ (green lines in Fig. 2). The density current, intruding between the upper and lower layers, can be clearly observed in Fig. 2(a), as well as the deflection of the pycnocline ahead of the nose of the intrusion shows the generation of the ISW (at $T^* = 25.2$ and $x^* = x/x_0 = 9.8$). The intrusion head and body regions are characterized by the presence of turbulent shear instabilities at both the interfaces with the ambient, in the form of clearly discernible Kelvin–Helmholtz billows [Figs. 2(a) and 2(b)]. Once the ISW completely detaches from the IGC, it flows downstream with an approximately constant celerity [Fig. 2(b)]. At later times, the ISW reaches the right-wall of the domain [Fig. 2(c)], and once reflected, it starts to flow backward interacting with the counter current [Fig. 2(d)].

The flow dynamics can be also clearly detected by drawing in the x–t plane the Hövmoller diagram of $\langle\rho^*\rangle$ [run P1H1X2D0 in Fig. 3(a)]. The relatively short initial lock length ($x_0 = 0.050$ m for run P1H1X2D0) allows us to observe the flow features for several lock-lengths (up to ~$43x^*$). The plot refers to the constant depth $y^* = y/H = 0.8$ in order to analyze the processes occurring at the pycnocline region. Looking at the lower part of Fig. 3(a), the thick diagonal white streak shows the propagation of the ISW downstream. Once reached the end of the domain, it is reflected by the solid wall [at $T^* = 109.3$, Fig. 3(a)] and starts to flow backward. It reaches the left wall of the domain at $T^* \sim 213$ undergoing reflection again along the positive x-axis direction. The evolution in time of the nose of the intrusion is identified by the gray streak dividing the plot in a predominantly black region (bottom-right part of the figure) from the rest of the gray-shaded graph.

The propagation of the ISW trough [$x_{fT}(t)$] is also evaluated through the analysis of $\langle\rho^*\rangle$ in the x–y plane by following the minimum of the pycnocline deflection ahead the IGC. Similarly, the evolution in time of the front position of the intrusion [$x_f(t)$] is inferred on the x–y plane by considering the convergence of the iso-density levels $\langle\rho^*\rangle = 0.1$ and $\langle\rho^*\rangle = 0.9$. The evolution of both the IGC front and ISW trough, derived by the instantaneous density fields, is then superimposed on the Hövmoller diagram in Fig. 3(a) (as red circles and green triangles, respectively), showing a good agreement with the shade analysis method.

As the length of the domain is sufficiently large in comparison with x_0, a secondary ISW also forms ahead of the intrusion, when the IGC front reaches the streamwise distance $x^* \sim 23$. The

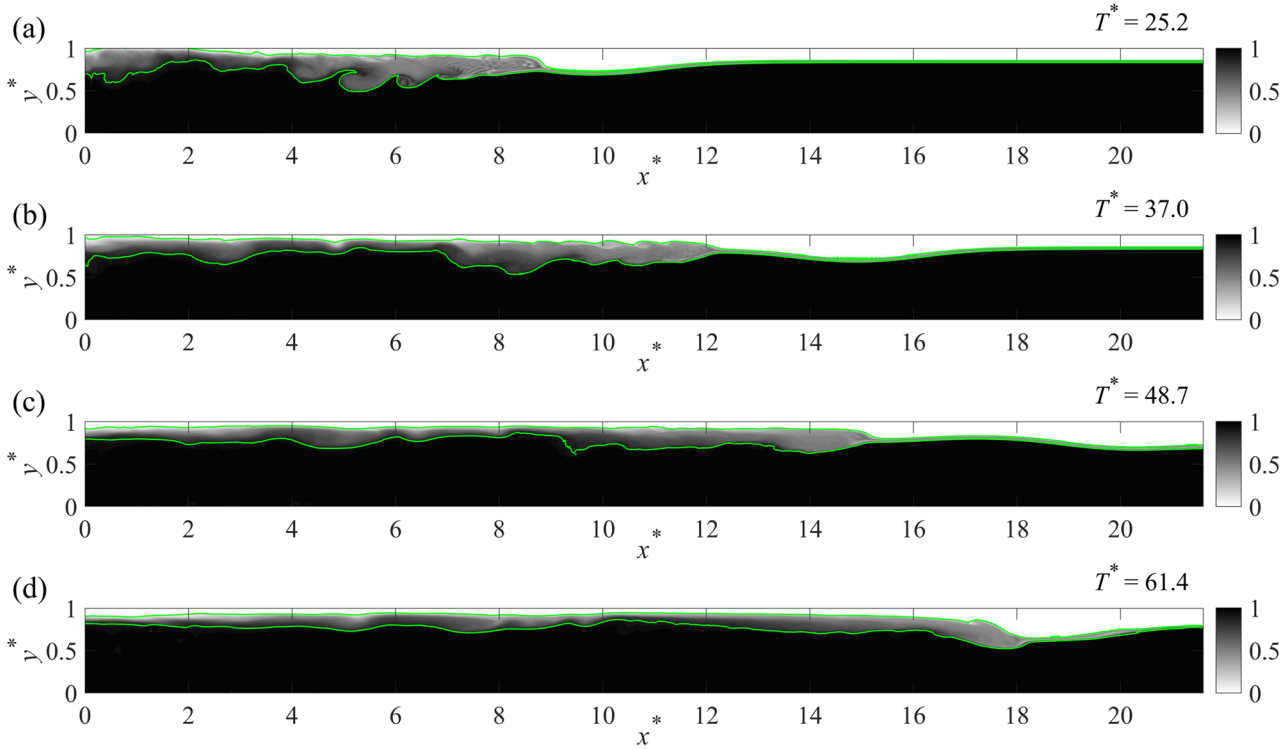

FIG. 2. Spanwise-averaged dimensionless density field at different times for P1H1X1D0 ($h_2 = 0.005$ m, $h_1 = 0.030$ m, $x_0 = 0.100$ m, $\rho_0 = 1000$ kg/m^3, $\rho_1 = 1020$ kg/m^3, and $\rho_2 = 1040$ kg/m^3): (a) $T^* = 25.2$; (b) $T^* = 37.0$; (c) $T^* = 48.7$; and (d) $T^* = 61.4$. Green contour shows $\langle\rho^*\rangle = 0.1$ and $\langle\rho^*\rangle = 0.9$.

Published under license by AIP Publishing

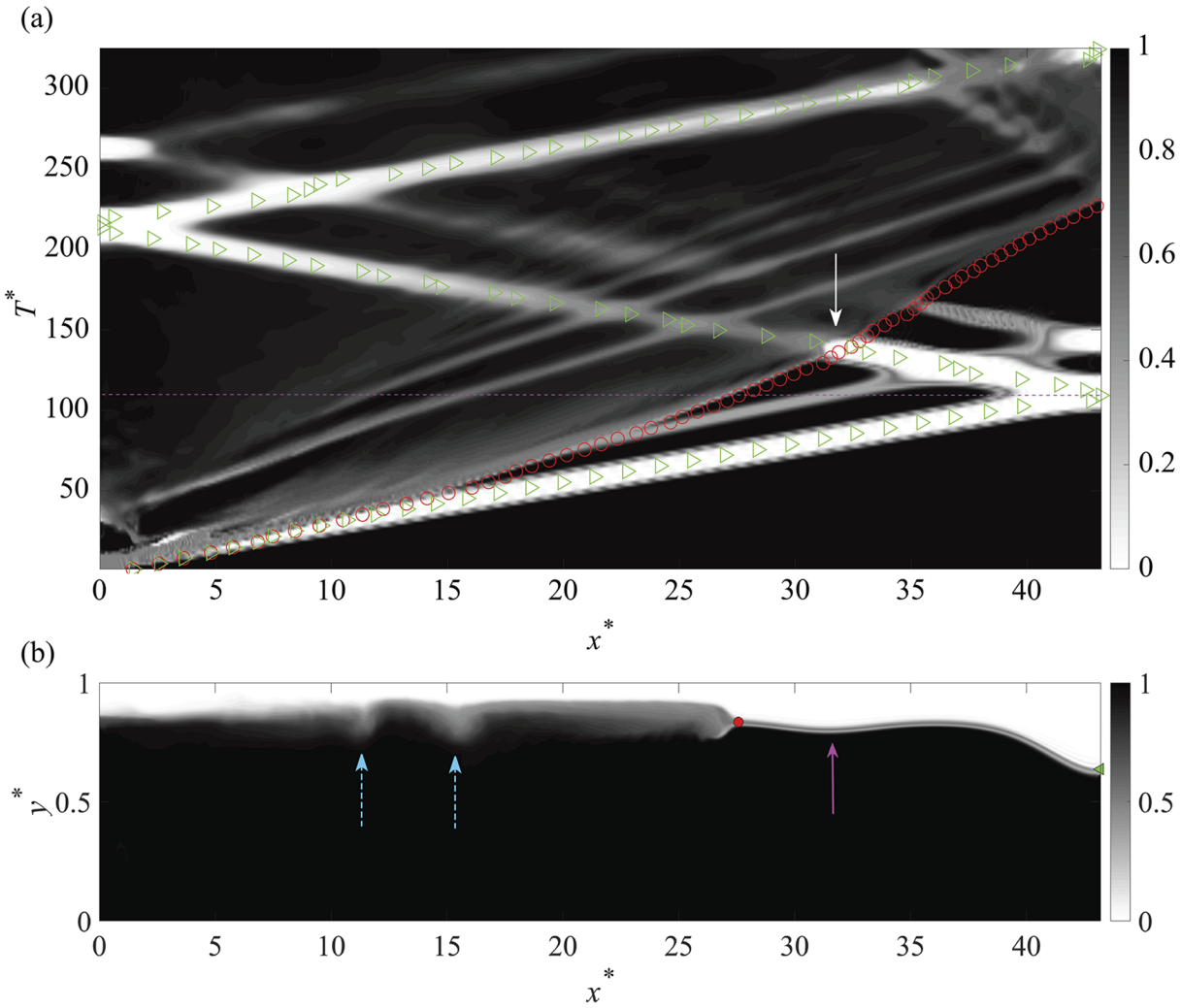

FIG. 3. (a) Hövmoller diagram in the x–t plane of $\langle \rho^* \rangle$ for P1H1X2D0 (h_2 = 0.005 m, h_1 = 0.030 m, x_0 = 0.050 m, ρ_0 = 1000 kg/m^3, ρ_1 = 1020 kg/m^3, ρ_2 = 1040 kg/m^3) at the constant depth y^* = 0.8. Magenta dashed line indicates T^* = 109.3. Red circles mark the front position of the IGC. Green triangles show the advancement in time of the ISW trough. White arrow indicates the ISW–IGC collision at T^* = 139.5. (b) $\langle \rho^* \rangle$ for P1H1X2D0 at T^* = 109.3. Red circle and green triangle mark the IGC front and the ISW trough, respectively. Magenta arrow indicates the formation of a secondary ISW ahead the IGC. Dashed cyan arrows signify the presence of trailing internal waves.

generation of more than one ISW from the same buoyant source is coherent with the ISW trains generally observed in nature[5,8,9] and in laboratory experiments.[36] A train of five rank-ordered ISWs propagates in the body and tail regions of the intrusion [gray diagonal streaks at about 15 < x^* < 20 and 100 < T^* < 150 in Fig. 3(a)]. Most of the main structures of the flow described are visible in the spanwise-averaged density field for the vertical x–y plane at T^* = 109.3 [i.e., the dashed magenta line in Figs. 3(a) and 3(b)]. The ISWs trapped into the current body [dashed cyan arrows in Fig. 3(b)] are relatively smaller than those ahead of its front [solid magenta arrows in Fig. 3(b)], and they are observed to propagate relatively slower, with an approximately constant celerity.

The stratification of the ambient fluid, for fixed released volumes, affects both the intrusion behavior and the wave's features. All our LESs represent intrusions characterized by $\varepsilon < 0$, and their behavior is asymmetric with respect to the pycnocline. In particular, the intrusion propagates mainly in the upper layer, and the head is just above the middle layer.[29] This asymmetry is enhanced for smaller ε [i.e., for D2 runs, Fig. 4(c)] and is less evident when ε get closer to zero [i.e., for D1 runs, Fig. 4(a)]. As a consequence, the resulting ISW is relatively larger in D2 runs than in D1 runs (Fig. 4).

B. ISWs characterization

The ISW amplitude, A_w, is evaluated as the vertical displacement between the wave trough and the initially unperturbed isodensity level $\langle \rho^* \rangle$ = 0.5 [Fig. 4(b)]. Following Sutherland, Barrett, and

Published under license by AIP Publishing

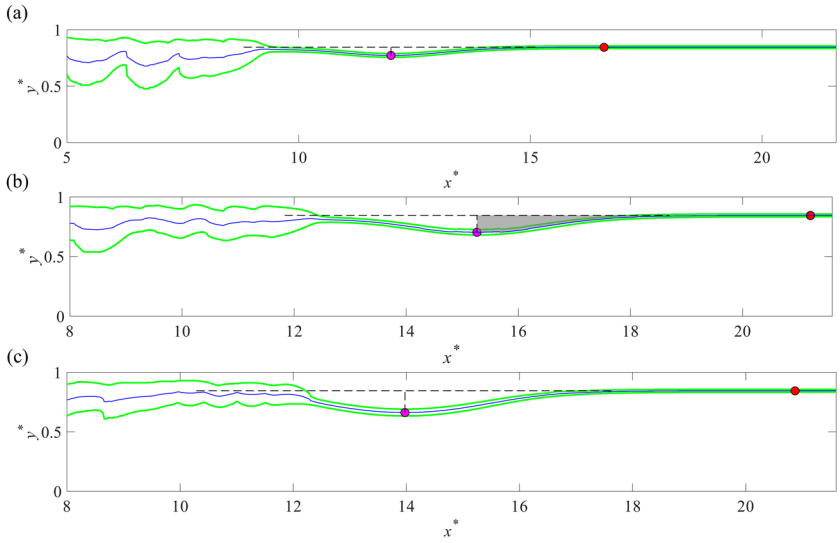

FIG. 4. Behavior of the flow for varying density gradients: IGC shape and ISW features. Green contour refers to $\langle\rho^*\rangle = 0.1$ and $\langle\rho^*\rangle = 0.9$. Blue contour is for $\langle\rho^*\rangle = 0.5$. Magenta and red dots mark the ISW trough and the first point vertically displaced from the undisturbed interface depth, respectively. (a) P1H1X1D1 (ρ_0 = 1000 kg/m^3, ρ_1 = 1020 kg/m^3, and ρ_2 = 1030 kg/m^3). (b) P1H1X1D0 (ρ_0 = 1000 kg/m^3, ρ_1 = 1020 kg/m^3, and ρ_2 = 1040 kg/m^3); gray filled area indicates the ISW half-surface (i.e., $S_w/2$). (c) P1H1X1D2 (ρ_0 = 1010 kg/m^3, ρ_1 = 1020 kg/m^3, and ρ_2 = 1040 kg/m^3).

Ivey,[14] the wave length is evaluated as

$$L_w = 2\frac{S_w}{A_w}, \tag{14}$$

where S_w is the ISW area [see gray filled area in Fig. 4(b)]. We identified the first point, along the pycnocline, vertically displaced with respect the initial (i.e., undisturbed) interface depth [red circle in Fig. 4(b)]. The included area in the pycnocline region between this point and the trough of the wave is defined as $S_w/2$.

For all runs, we analyze how the main normalized ISWs geometric features (i.e., $A_w{}^* = A_w/H$, $L_w{}^* = L_w/H$, and $S_w{}^* = S_w/H^2$) change with the stratification of the ambient fluid (i.e., vs Δ and ε in Figs. 5 and 6, respectively). The length of the wave increases if the upper layer widens, as proved by the linear trend between $L_w{}^*$ and Δ, when other parameters are fixed [circles, triangles, and diamonds in Figs. 5(a) and 6(a)]. This can be explained by considering that $L_w{}^*$ actually represents the quantity used to define the shallow-water condition $L_w/H > 1$.[15,55] Indeed, for deeper pycnoclines (i.e., larger Δ), the ISWs feel the bottom more significantly, and they assume a wave profile characterized by larger L_w. The pycnocline thickness, instead, poorly affects $L_w{}^*$, $A_w{}^*$ and $S_w{}^*$ (black circle, square, and star in Figs. 5 and 6) in agreement with la Forgia *et al.*[36] However, a decreasing trend of $L_w{}^*$ can be detected when the pycnocline widens [Figs. 5(a) and 6(a)]. The relative density difference between the intrusion and the ambient layers significantly affects both $A_w{}^*$ and $S_w{}^*$: when the IGC initiates the motion intruding at lower depths, larger ISWs are generated [clear gray symbols, black symbols, and dark-gray symbols in Figs. 5(b), 5(c), 6(b), and

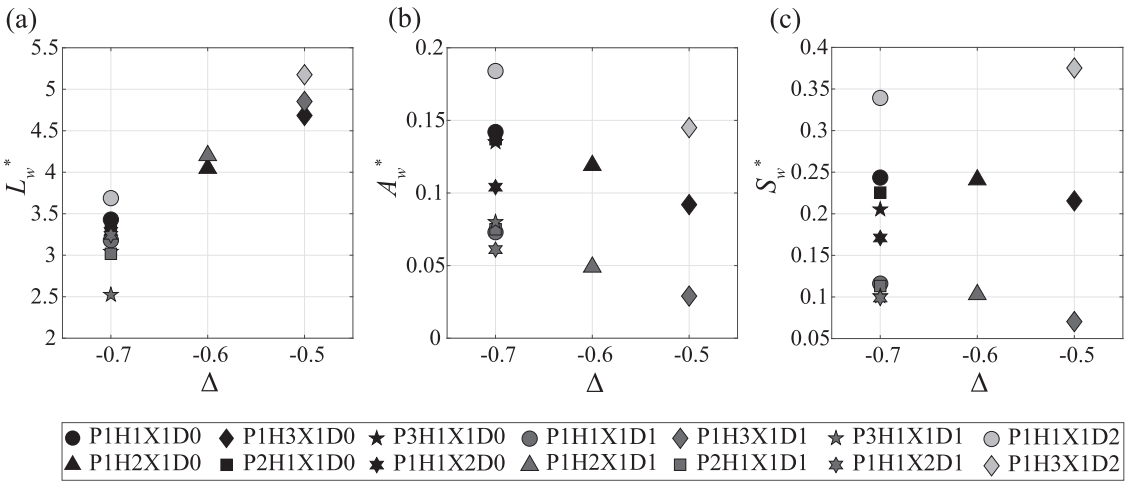

FIG. 5. Features of the ISWs vs Δ: (a) $L_w{}^*$; (b) $A_w{}^*$; and (c) $S_w{}^*$.

Published under license by AIP Publishing

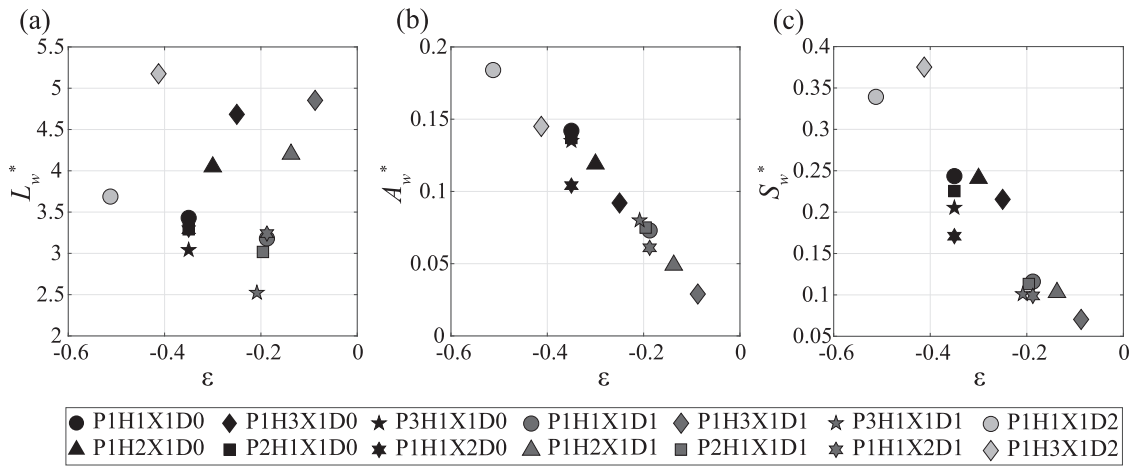

FIG. 6. Features of the ISWs vs ε: (a) $L_w{}^*$; (b) $A_w{}^*$; and (c) $S_w{}^*$.

5(c)]. In particular, an almost linear dependence between $A_w{}^*$ and ε can be observed in Fig. 6(b). As expected, also the initial lock position (i.e., in the present case, the initial volume of the release) affects the wave dimension, influencing $A_w{}^*$ [circles and hexagrams in Figs. 5(b) and 6(b)] and $S_w{}^*$ [circles and hexagrams in Figs. 5(c) and 6(c)].

For each run, we also estimated the ISW mean celerity as the slope of the linear function best fitting the x_{fT} data. The evolution in time of the trough position is inferred for three successive phases of each numerical experiment: the first goes from the formation of the wave to its reflection to the right-end of the domain (characterized by a mean celerity v_1); the second phase refers to the wave propagating counter the current, i.e., from the right-end of the domain leftward (with a mean celerity v_2); the third phase corresponds to the propagation of the wave along the positive x-axis direction, until it reaches again the right-end side of the domain (with mean celerity v_3).

During the three phases, the ISWs behavior can be considered as almost completely bi-dimensional, and no three-dimensional patterns were observed to develop along the spanwise direction.

ISWs celerities, normalized by the buoyancy velocity u_b, are herein denoted by a superscript asterisk (*).

We observe that the variation of the ambient stratification deeply affects $v_1{}^*$. In particular, the density asymmetry of the system rules the ISWs celerities and waves in D2 runs move faster than in the other configurations (i.e., clear gray symbols in Fig. 7).

The thickness of the upper layer h_1, only partially affects $v_1{}^*$: all other conditions being equal, the increase of Δ is associated with slightly faster waves [see circles, triangles and diamonds in Fig. 7(a)]. Moreover, the increase in the pycnocline thickness h_2 causes a decrease in $v_1{}^*$ [see circles, squares and stars in Figs. 7(a) and 7(b)].

The higher celerity of the waves in D2 cases is clearly evident also in the plot $v_1{}^*$ vs ε, where an approximately linear trend can be detected among cases characterized by similar geometric initial conditions and different density gradients [e.g., clear gray, black, and dark-gray circles in Fig. 7(b)]. This can be explained by considering that ε represents the asymmetry of the system: for $\varepsilon = 0$, the fluid released from the lock has a density equal to the depth-averaged density of the ambient. Under this condition, ahead of the intrusion nose, no deflections of the pycnocline are observed, and the IGC velocity is at minimum,[34,35] as deeper discussed in the following Sec. III C. Thus, the lower the ε, the greater the asymmetry and the faster the wave celerity.

The sole effect of the ISWs amplitude can be crucially detected by comparing D1 and D2 cases [see dark-gray symbols and clear gray symbols in Fig. 7(b)], both characterized by the same density difference ahead of the ISWs: larger celerities are observed for waves with larger amplitudes.

We focused on the relation between celerities $v_2{}^*$ and $v_3{}^*$ with respect to $v_1{}^*$ [Figs. 7(c) and 7(d), respectively]. The mean celerity of the wave after the reflection on the right-end of the domain is always larger than the mean celerity of the incident wave [i.e., $|v_2{}^*| > v_1{}^*$ in Fig. 7(c)]. Contrary to what one could have expected, ISWs engaging with intrusions not only do not lose their energy but are observed to increase their celerity. This occurrence was also observed in the laboratory experiments of la Forgia *et al.*,[36] who noticed that for some cases, although the wave broke on the sloping boundary, the reflected wave traveled faster than the one before the breaking event. For our numerical simulations, the presence of a vertical wall at the end of the domain leads the incoming wave to be totally reflected, without any evidence of turbulent instability. However, the waves are observed to slightly decrease their celerity during the interaction with the wall and the increase in $|v_2{}^*|$ is definitely related to the interaction with the intrusion. When the reflected wave collides with the rightward propagating IGC, the ISW is compressed upward, due to the presence along its path of the intrusion head, which, in turn, is pushed to lower depths. Since the wave is restricted to a thinner section, it loses its original shape and increases its celerity up to values higher than the ones observed during the incident wave phase. Furthermore, the velocity field around the head of the intrusion, characterized by the presence of anticlockwise billows in the upper layer, propagates in the same direction of the reflected wave, enhancing its celerity (see Sec. III D). At following times, as the

Published under license by AIP Publishing

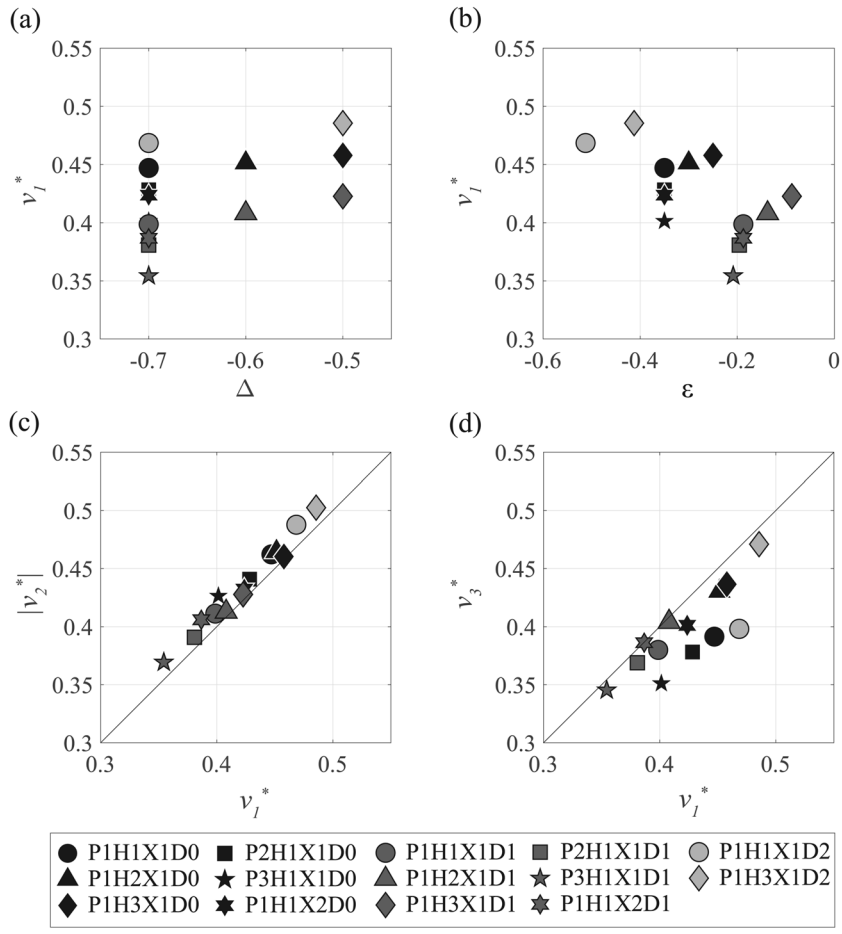

FIG. 7. ISWs celerities: (a) $v_1{}^*$ vs Δ; (b) $v_1{}^*$ vs ε; (c) absolute value of $v_2{}^*$ vs $v_1{}^*$; and (d) $v_3{}^*$ vs $v_1{}^*$.

ISW is reflected by the left vertical wall, it rearranges itself and starts to flow rightward again. Interestingly, in this third phase, the wave celerity decreases with respect to both $v_1{}^*$ and $|v_2{}^*|$, possibly due to no longer receiving additional boosts from the intrusion [Fig. 7(d)]. We highlight that while during the first rightward journey, the wave propagates freely, a number of positive phase shifts with smaller internal waves occur on the leftward journey. On the other hand, on the second rightward journey (third phase), the primary solitary wave has few interactions with smaller solitary waves and therefore fewer phase shift boost. This causes v_3^* to be significantly reduced with respect to v_2^*. It must also be pointed out that in an ideal free propagation condition, dissipation plays a role in reducing the wave celerity and geometrical features: the waves are expected to progressively decrease their features traveling along the domain. While this seems to not occur during the second phase, it becomes evident in the third journey, as the wave has already traveled long distances and it does not receive the additional boost of the IGC.

C. IGCs front evolution

Lock-release gravity currents are characterized by an initial phase during which the front propagates at an almost constant speed, followed by a second phase during which the front decelerates.[18] In IGCs, the presence of a initial constant velocity phase was observed in different studies, and the value of this velocity was linked to the density gradients driving the motion and to the geometric setting of the ambient with respect to the intrusion characteristics.[33–35]

The behavior and the dynamics of the IGC are, indeed, strongly affected by the ambient stratification. This can be observed in the evolution of the dimensionless front position of the intrusion, $x_f^* = (x_f - x_0)/x_0$, vs the dimensionless time T^* (Fig. 8) and in the evolution of the front velocity V_f. The latter is evaluated as the first derivative of $x_f(t)$ and made non-dimensional with u_b (Fig. 9). The presence of an almost constant speed of the intrusion front after which the current decelerates can be observed also in our LESs (Figs. 8 and 9). In fact, while ISWs are observed to be almost completely 2D, the development of 3D patterns is observed at the IGCs interface, especially after the slumping phase: turbulent dissipative structures evolve, causing the current to decelerate. In particular, we found that fixing all other variables, variation in the upper layer thickness causes a reduction in the intrusion velocity [circles, triangles, and diamonds in Figs. 8(a) and 9(a)]. The increase in the pycnocline thickness [Figs. 8(b) and 9(b)], in the range of the present

Published under license by AIP Publishing

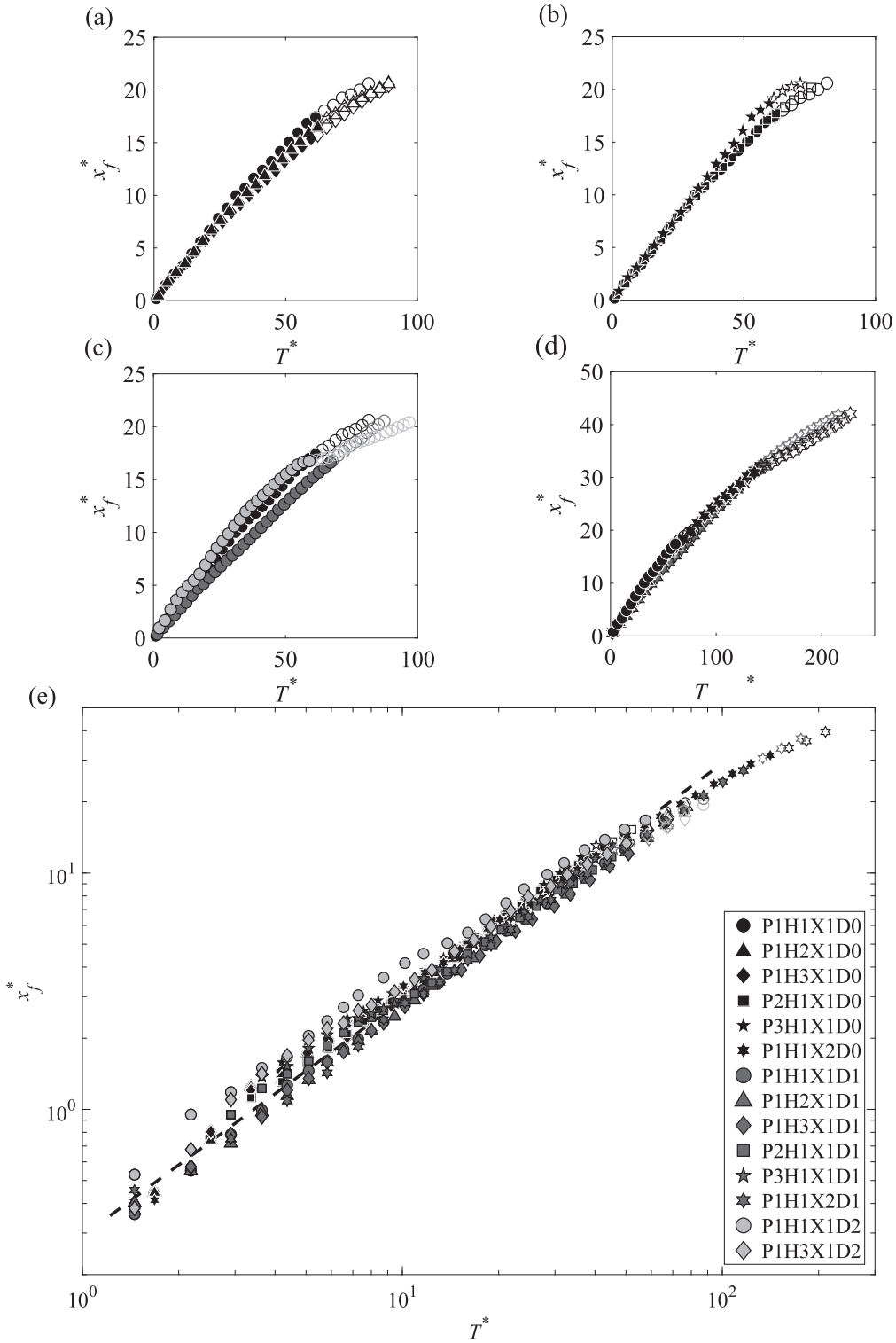

FIG. 8. Time evolution of the dimensionless front position of the IGCs: (a) influence of the upper-layer thickness, h_1; (b) influence of the pycnocline thickness, h_2; (c) comparison between runs characterized by different density gradients; (d) comparison between runs with different x_0; and (e) x_f^* vs T^* for all runs in a log–log scale. Filled and empty markers refer to the IGC propagation before and after the interaction with the ISW, respectively.

Published under license by AIP Publishing

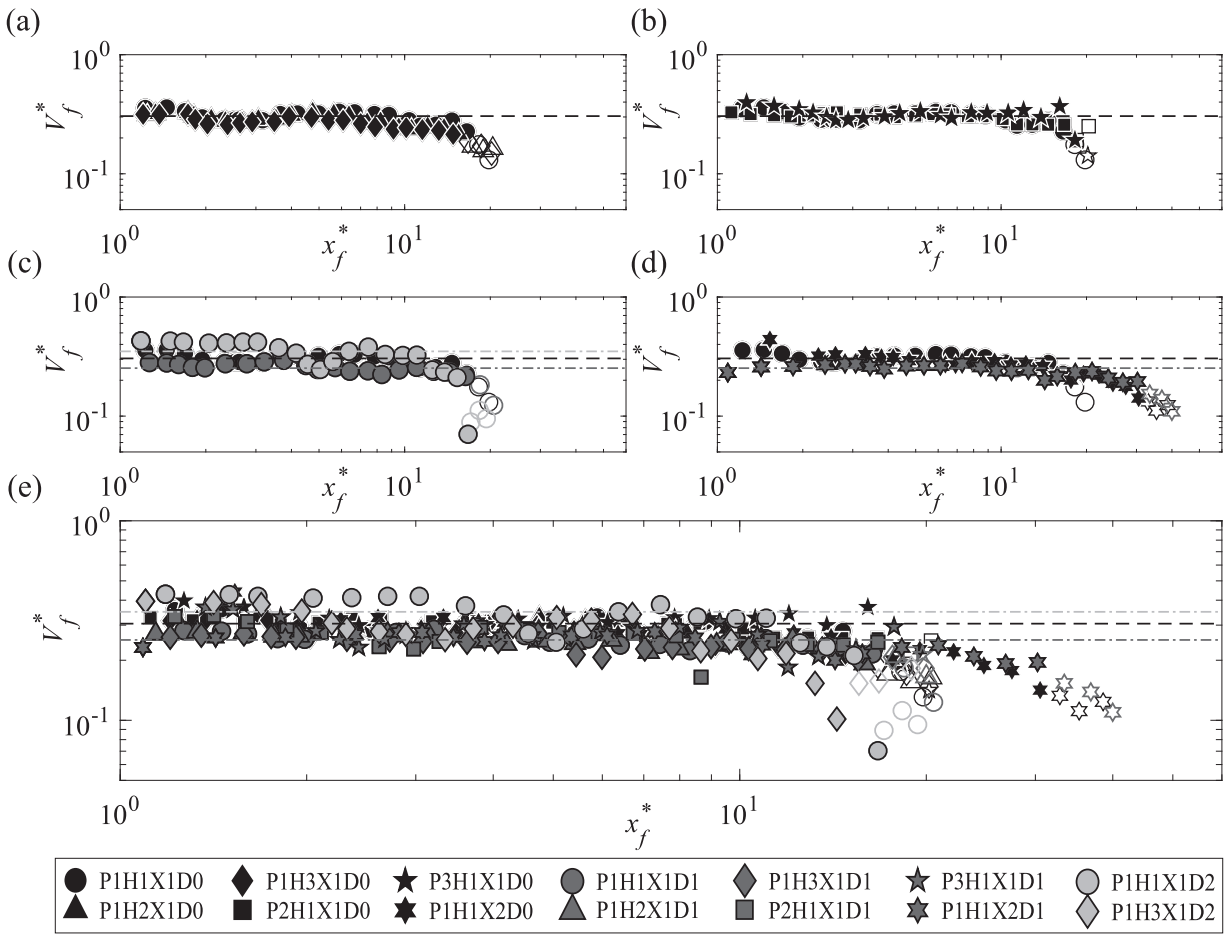

FIG. 9. Time evolution of the dimensionless front velocity of the IGCs in log–log scale: (a) influence of the upper-layer thickness, h_1; (b) influence of the pycnocline thickness, h_2; (c) comparison between runs characterized by different density gradients; (d) comparison between runs with different x_0; (e) V_f^* vs x_f^* for all runs. Filled and empty markers refer to the IGC propagation before and after the interaction with the ISW, respectively. Horizontal lines mark the constant velocity value predicted by the model of Cheong, Kuenen, and Linden:[34] black dashed lines refer to the D0 runs, dark-gray dashed-dotted lines mark the D1 runs, and clear gray dashed-dotted lines signify the D2 runs.

study, only poorly affects the initial speed of the current: IGCs in P1 runs initially propagate slightly faster than in P3 runs.[33,36] Furthermore, differences in the duration of the constant velocity phase can be clearly observed: passing from an almost two-layer ambient (i.e., P1 runs) up to a three-layer ambient (i.e., P2 and P3 runs), the front retains an approximately constant speed longer [Figs. 8(b) and 9(b)]. In fact, the interface between the IGC and the ambient is smoother for P3 runs than for P1 runs, and turbulent instabilities are reduced; a larger intermediate layer enhances the IGCs inertia, inducing a less dissipating behavior, in agreement with what was experimentally observed by la Forgia *et al.*[36] We notice that the most significant changes in the IGCs front evolution occur when varying ambient densities. By comparing D1, D0, and D2 runs, a decrease in the front speeds during the initial phase of the IGCs is clearly visible [Figs. 8(c) and 9(c)]. As expected, we observe that a decrease in the upper (D2 runs) or in the lower (D1 runs) density gradient (i.e., g'_{iU} and g'_{Li}) acts differently with respect to the symmetrical density case (D0 runs). This can be explained considering that the IGC, also in the D0 runs, is not double symmetric, i.e., its density is never the depth-weighted mean density of the ambient. Thus, by reducing g'_{iU} (g'_{Li}), we never reached a symmetric condition, but we enhanced (mitigated) the whole asymmetry of the system. The variation of x_0 also affects IGCs dynamics [Figs. 8(d) and 9(d)]. For smaller x_0, the volume released decreases, and the IGC flows for longer dimensionless distances before interacting with the reflected ISW. This allows the observation of a deceleration of the IGC independently of the ISW dynamics. The collision between the ISW and the IGC can also act by partially reducing the IGC speed. In fact, once the IGC catches up with the ISW, finding an obstacle to its path, it deepens within the lower layer, following the ISW-induced pycnocline displacement. Consequently, the front velocity is reduced both for the interaction with the ISW and for the natural dissipation of

Published under license by AIP Publishing

the IGC. The x_f^* and V_f^* plots, for X2 runs, clearly mark the presence of a deceleration phase of the IGC, whose development can be seen only in its beginning for all others in X1 runs [Figs. 8(d) and 9(d)].

Differences observed in the initial IGC speed can be explained by comparing the pycnocline position set for each run (denoted as h_3 in Fig. 1), and the hypothetical depth that the pycnocline should have if a symmetric intrusion would be released (i.e., an intrusion of density equal to the depth-weighted mean density of the ambient). In fact, by following Flynn and Linden[35] and Cheong, Kuenen, and Linden,[34] we define the equilibrium height h_e^*,

$$h_e^* = \frac{h_e}{H} = \frac{g'_{iU}}{g'_{LU}}. \tag{15}$$

It was found that the speed of the intrusion is at minimum when the IGC is symmetric;[34,35] in this view, the more the pycnoline depth of our runs approaches the equilibrium height, the more the resulting intrusion velocity is observed to decrease. By comparing cases characterized by the same density gradients (e.g., D0 runs), an increase in the upper layer thickness acts moving the pycnocline position closer and closer to the equilibrium depth (i.e., $h_e = H/2$ for D0 runs, with the pycnocline depth $h_3 = 0.85H$, $h_3 = 0.80H$, and $h_3 = 0.75H$ for H1, H2, and H3 runs, respectively). Similarly, for fixed upper layer thickness (e.g., H1 runs and $h_3 = 0.85H$), by varying the buoyancy density gradients, the equilibrium depth h_e changes (i.e., $h_e = 1/3H$, $h_e = 1/2H$, and $h_e = 2/3H$ for D2, D0, and D1 runs, respectively) and consequent variations in the IGC speed occur. Following Cheong, Kuenen, and Linden[34] formulation, the values attended during the constant velocity phase of the IGC can be evaluated, V^*_{fCH06}, and they are shown in Fig. 9 for P1H1X1D0, P1H1X1D1, and P1H1X1D2 cases (black dashed lines, dark-gray dashed-dotted lines, and clear gray dashed-dotted lines, respectively). Theoretical predictions are in agreement with our simulations. Velocities are also predicted to vary less incisively when only the upper layer thickness is varied (e.g., $0.279 \le V^*_{fCH06} \le 0.305$ for P1H1X1D0, P1H2X1D0, and P1H3X1D0 cases), in agreement with what observed by LESs.

D. Flow field

We investigate the flow field by the analysis of the spanwise-averaged components of the velocity vector along the streamwise, vertical, and spanwise directions, normalized by u_b (i.e., $\langle u^* \rangle$, $\langle v^* \rangle$, and $\langle w^* \rangle$, respectively). The spanwise-averaged vorticity $\langle \omega^* \rangle$, made dimensionless with x_0/u_b, was also computed (Fig. 10). During the IGC propagation along the tank, high values of $\langle u \rangle$ are observed in the head and body regions of the intrusion as well as within the preceding ISW [Fig. 10(a)]. For continuity, backward propagating heavy fluid is clearly visible in the ambient, particularly below the ISW trough and the IGC body [i.e., negative values of $\langle u^* \rangle$ in Fig. 10(a)]. Kelvin–Helmholtz instabilities developing at the IGC interface are characterized by a relatively large vorticity [Fig. 10(b)]. As expected, counter-clockwise vortices develop at the upper-layer interface of the IGC [i.e., positive $\langle \omega^* \rangle$ in Fig. 10(b)], and clockwise vortices form at the lower-layer interface of the IGC [i.e., negative $\langle \omega^* \rangle$ in Fig. 10(b)]. On the other hand, during the propagation of the ISW, although the significant values observed for $\langle u^* \rangle$, no additional vorticity develops along the wave profile [i.e., $\langle \omega^* \rangle \sim 0$ in Fig. 10(b)]

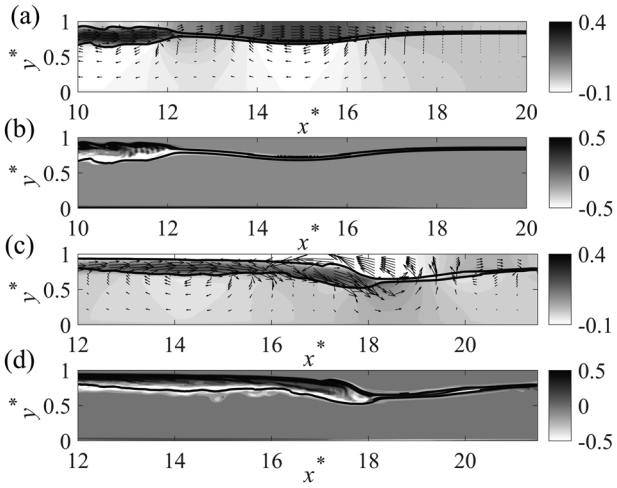

FIG. 10. Dimensionless velocity and vorticity fields at different times for P1H1X1D0 ($h_2 = 0.005$ m, $h_1 = 0.030$ m, $x_0 = 0.100$ m, $\rho_0 = 1000$ kg/m^3, $\rho_1 = 1020$ kg/m^3, and $\rho_2 = 1040$ kg/m^3): (a) $\langle u^* \rangle$ at $T^* = 37.0$; (b) $\langle \omega^* \rangle$ at $T^* = 37.0$; (c) $\langle u^* \rangle$ at $T^* = 61.4$; and (d) $\langle \omega^* \rangle$ at $T^* = 61.4$. Black contour refers to $\langle \rho^* \rangle = 0.1$ and $\langle \rho^* \rangle = 0.9$.

and negative values of $\langle \omega^* \rangle$ can be observed only within the thin pycnocline. After the ISW reflection on the right-end of the domain, the interaction between the IGC and the ISW occurs [Figs. 10(c) and 10(d)]. At this stage, the flow moves in the counter-clockwise direction: the IGC deepens and the ISW passes over the intrusion head. The backward values of $\langle u^* \rangle$ of the ISW agree with the velocity field developed in the upper-layer ambient over the IGC head, causing an increase in the ISW celerity [Fig. 10(c)]. Moreover, the ISW is constrained to pass through a thinner upper layer partially occupied by the IGC, and an increase in the ISW speed occurs for continuity. Also, the positive values of $\langle \omega^* \rangle$ along all the IGC body cause the increase of the ISW kinetic energy as it propagates leftward [Fig. 10(d)]. However, once the ISW reaches the left-end of the domain, it loses the previously enhanced energy and is observed to propagate rightward with a relatively lower celerity, which now uniquely depends on the density structure it is propagating through.

We evaluate the ISW-induced flow rate through the upper layer. We consider the spanwise-averaged flow rate of the system $q(x, y, t) = \langle u \rangle dy(y)$, along the streamwise direction, for each cell of the domain. Then, we evaluated the total flow rate, $Q_t(x, t)$, passing over the isodensity level $\langle \rho^* \rangle = 0.1$. By plotting the Hövmoller diagram of the dimensionless flow rate passing in the upper layer, $Q_t^* = Q_t(x,t)/(u_b H)$, the propagation of the ISW along the domain can be clearly discerned (i.e., non-zero values of Q_t^* in Fig. 11). The global trend of Q_t^* shows that the order of magnitude of the flow rate related to the passage of the ISW is conserved in mean during the simulation. This confirms that during the interaction between an ISW and an IGC, the reduction of the available area for the wave to overtake the counter current largely determines the flow dynamics. However, small variation of Q_t^* can be observed during the three passages of the ISW along the domain (Fig. 11).

Published under license by AIP Publishing

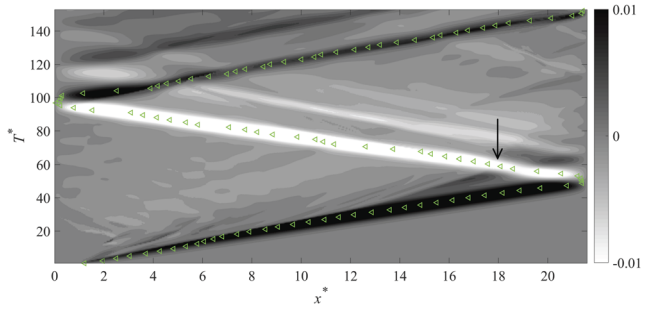

FIG. 11. Hövmoller diagram of the dimensionless flow rate Q_t^* for P1H1X1D2 (h_2 = 0.005 m, h_1 = 0.030 m, x_0 = 0.100 m, ρ_0 = 1010 kg/m^3, ρ_1 = 1020 kg/m^3, and ρ_2 = 1040 kg/m^3). Green triangles mark the evolution of the ISW trough, $x_{fT}(t)$. Black arrow indicates the ISW–IGC collision at T^* = 59.7.

To better investigate this phenomenon, we evaluated the quantity $Q(t)$, defined as the total flow rate passing in the upper layer in correspondence of the ISW trough, i.e., in a vertical plane of reference moving with $x_{fT}(t)$ (Fig. 12). The comparison of $Q(t)$ evaluated for the different runs shows that for increasing values of the upper layer H_1, the mean flow rate over the ISW decreases because the mean value of the streamwise velocity field $\langle u \rangle$ decreases [Fig. 12(a)]. Similarly, the increase in the middle-layer thickness, h_2, is related to a decrease in $Q(t)$ [Fig. 12(b)]. Changes in the ambient density cause a variation in the flow rate following a similar trend of the IGC front velocities: D2 runs are characterized by larger $Q(t)$ magnitude with respect to D0 and D1 runs [Fig. 12(c)]. When lower volumes are released (i.e., for reducing x_0), a decrease both in the ISWs geometric features and in the related velocity field is observed [Fig. 12(d)]. For all runs, the flow rate is approximately conserved during the first two passages of the ISWs along the domain: after the interaction with the IGC, absolute values of $Q(t)$ are equal or larger than those observed during the first positive x-axis propagation. This confirms that the interaction with the IGC gives the ISW an additional push, both due to the decrease of the available area in the upper layer to its flow and for the interaction of the ISW and IGC velocity fields at the interface. After the ISW reaches the left wall of the domain and restarts to flow along the positive x-axis direction, the additional push vanishes, and both ISW celerity and $Q(t)$ significantly decrease (Fig. 12).

IV. CONCLUSIONS

In specific, geographic configurations, such as in closed basins, lochs, and lakes, the ISWs generated by river plumes are observed to reach the opposite shore and reflect against the same current that generated them. We performed LESs in order to reproduce and analyze, in a laboratory-scale domain, the dynamics of IGCs generating ISWs, as well as their interaction.

The uniform lock fluid, interacting with the stratified ambient, flows as an IGC propagating in correspondence of the intermediate layer. A clear displacement of the pycnocline occurs ahead of the intrusion, signifying the generation of an ISW. The latter, propagating faster than the intrusion, detaches from it and reaches the right-end of the domain where it is reflected by the vertical wall. Then, it flows along the negative x-axis direction colliding against the IGC. During the interaction, the ISW is pushed upward by the intrusion, which, in turns, flows under the wave moving at larger depth. We observed a significant reduction in the upper layer thickness because the area available for the ISW propagation is partially occupied by the intrusion. Moreover, at the upper interface, the IGC-induced velocity field acts facilitating the wave propagation. For these reasons, the wave celerity is enhanced as it propagates above the intrusive current.

As expected, ISWs main features are affected by the ambient stratification. In particular, the increase in the relative flow depths of the upper and lower layer, Δ, causes an increase in the ISW length, while an increase in the relative density difference between the intrusion and the ambient, ε, causes a reduction in the ISW amplitude, surface, and celerity. Consequently, LESs show that in D2 runs, ISWs have the greatest amplitude and celerities, while in $H3$ runs (i.e., cases with the largest upper layer thickness), ISWs have the

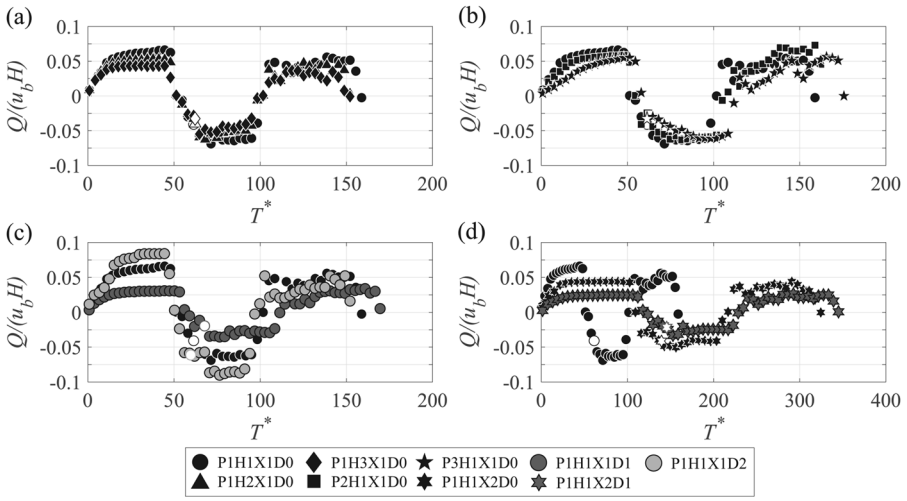

FIG. 12. Flow rate passing in the upper layer in a vertical plane of reference moving with $x_{fT}(t)$. (a) Comparison among runs with varying H_1; (b) comparison among runs with varying h_2; (c) comparison among runs with varying density of the ambient; and (d) comparison among runs with varying x_0. Empty markers signify the time of the interaction between the ISW and the IGC.

Published under license by AIP Publishing

greatest length. We observe that after the reflection, the ISW flows faster along the negative x-axis direction if compared to the previous phase (i.e., $|v_2^*| > v_1^*$ for all runs). Then, after the reflection on the left-end of the domain, the ISW looses its additional push given by the interaction with the IGC and propagates along the positive x-axis direction with $v_3^* < v_1^*$.

The characteristics of the intrusions are also affected by the parameters varied in the present simulations, consistently with what found for ISWs. We observe that by increasing the asymmetry of the system (i.e., for smaller ε), IGC intrudes into the middle layer leaning to the upper layer more incisively. By analyzing the evolution in time of the front position of the IGC, we observe the presence of an initial phase during which the current moves at an almost constant velocity and a second phase during which the intrusion clearly decelerates. In agreement with previous studies,[34,35] we observe that the velocity of the intrusion, during the first phase, decreases if the pycnocline position set at the beginning of each run approximates the equilibrium depth. For this reason, the front velocity of IGCs in D2 runs is faster than the one in D0 runs and in D1 runs. Similarly, in H1 runs, the intrusion propagates faster than in H3 runs.

The main flow dynamics analyzed in the present study are only secondary affected by three-dimensional instabilities of the flow. In particular, IGCs developed three-dimensional patterns along the spanwise direction especially after the slumping phase. On the contrary, evolution of ISWs can be considered as completely bi-dimensional, not only during their propagation but also after their reflection on the right hand-side boundary. These evidences are in agreement with the dissipative behavior characterizing IGCs evolution and, in turns, with the approximatively conservative one commonly observed for ISWs.

The analysis of the velocity fields allows the detection of Kelvin–Helmholtz billows at the interface between the intrusion and the ambient. These turbulent structures gradually dissipate during the simulations. However, the velocity field in the intrusion surroundings acts to facilitate the passage of the ISW during their interaction. Furthermore, the analysis of the flow rate passing through a vertical section in the upper layer moving with the ISW trough indicates the crucial role played by the reduction of the area available to the ISW to overtake the IGC. In fact, since this quantity remains almost constant during the simulation, the increase in the ISW celerity can be mostly related to this area contraction the ISW has to flow through.

ACKNOWLEDGMENTS

This research was funded by the Italian Ministry of Education, University and Research (MIUR) through the Departments of Excellence 2018–2022 Program.

DATA AVAILABILITY

The data that support the findings of this study are available within the article.

REFERENCES

[1]J. E. Simpson, *Gravity Currents: In the Environment and the Laboratory* (Cambridge University Press, 1997).
[2]G. Valerio, M. Pilotti, C. L. Marti, and J. R. Imberger, "The structure of basin-scale internal waves in a stratified lake in response to lake bathymetry and wind spatial and temporal distribution: Lake Iseo, Italy," Limnol. Oceanogr. **57**, 772–786 (2012).
[3]W. Alpers, P. Brandt, A. Rubino, and J. O. Backhaus, "Recent contributions of remote sensing to the study of internal waves in the straits of Gibraltar and Messina," Dyn. Mediterranean Straits Channels **17**, 1–40 (1996).
[4]M. Des, M. deCastro, M. C. Sousa, J. M. Dias, and M. Gómez-Gesteira, "Hydrodynamics of river plume intrusion into an adjacent estuary: The Minho River and Ria de Vigo," J. Mar. Syst. **189**, 87–97 (2019).
[5]J. D. Nash and J. N. Moum, "River plumes as a source of large-amplitude internal waves in the coastal ocean," Nature **437**, 400 (2005).
[6]W. Alpers, P. Brandt, and A. Rubino, "Internal waves generated in the straits of Gibraltar and Messina: Observations from space," in *Remote Sensing of the European Seas* (Springer, 2008), pp. 319–330.
[7]L. C. Vilhena, C. L. Marti, and J. Imberger, "The importance of nonlinear internal waves in a deep subalpine lake: Lake Iseo, Italy," Limnol. Oceanogr. **58**, 1871–1891 (2013).
[8]D. Bourgault, P. S. Galbraith, and C. Chavanne, "Generation of internal solitary waves by frontally forced intrusions in geophysical flows," Nat. Commun. **7**, 13606 (2016).
[9]M. Toberman, M. Inall, T. Boyd, E. Dumount, and C. Griffiths, "Nonlinear internal waves and plumes generated in response to sea-loch outflow, AUV, and time-lapse photography observations," J. Geophys. Res.: Oceans **122**, 5522–5544, https://doi.org/10.1002/2016jc012208 (2017).
[10]S. A. Thorpe, A. J. Hall, and S. Hunt, "Bouncing internal bores of Ardmucknish Bay, Scotland," Nature **306**, 167–169 (1983).
[11]X. Xie, M. Li, and W. C. Boicourt, "Breaking of internal solitary waves generated by an estuarine gravity current," Geophys. Res. Lett. **44**, 7366–7373, https://doi.org/10.1002/2017gl073824 (2017).
[12]J. Wu, "Mixed region collapse with internal wave generation in a density-stratified medium," J. Fluid Mech. **35**, 531–544 (1969).
[13]J. Y. Holyer and H. E. Huppert, "Gravity currents entering a two-layer fluid," J. Fluid Mech. **100**, 739–767 (1980).
[14]B. R. Sutherland, K. J. Barrett, and G. N. Ivey, "Shoaling internal solitary waves," J. Geophys. Res.: Oceans **118**, 4111–4124, https://doi.org/10.1002/jgrc.20291 (2013).
[15]G. La Forgia, C. Adduce, and F. Falcini, "Laboratory investigation on internal solitary waves interacting with a uniform slope," Adv. Water Resour. **120**, 4–18 (2018).
[16]V. Lombardi, C. Adduce, and M. La Rocca, "Unconfined lock-exchange gravity currents with variable lock width: Laboratory experiments and shallow-water simulations," J. Hydraul. Res. **56**, 399–411 (2018).
[17]M. C. De Falco, L. Ottolenghi, and C. Adduce, "Dynamics of gravity currents flowing up a slope and implications for entrainment," J. Hydraul. Eng. **146**, 04020011 (2020).
[18]J. W. Rottman and J. E. Simpson, "Gravity currents produced by instantaneous releases of a heavy fluid in a rectangular channel," J. Fluid Mech. **135**, 95–110 (1983).
[19]G. La Forgia, C. Adduce, F. Falcini, and C. Paola, "Migrating bedforms generated by solitary waves," Geophys. Res. Lett. **46**, 4738–4746, https://doi.org/10.1029/2019gl082511 (2019).
[20]G. La Forgia, T. Tokyay, C. Adduce, and G. Constantinescu, "Bed shear stress and sediment entrainment potential for breaking of internal solitary waves," Adv. Water Resour. **135**, 103475 (2020).
[21]C.-S. Wu and A. Dai, "Experiments on two-layer stratified gravity currents in the slumping phase," J. Hydraul. Res. **57**, 1–14 (2019).
[22]L. Ottolenghi, C. Adduce, R. Inghilesi, V. Armenio, and F. Roman, "Entrainment and mixing in unsteady gravity currents," J. Hydraul. Res. **54**, 541–557 (2016).
[23]L. Ottolenghi, P. Prestininzi, A. Montessori, C. Adduce, and M. La Rocca, "Lattice Boltzmann simulations of gravity currents," Eur. J. Mech.: B/Fluids **67**, 125–136 (2018).
[24]G. La Forgia, T. Tokyay, C. Adduce, and G. Constantinescu, "Numerical investigation of breaking internal solitary waves," Phys. Rev. Fluids **3**, 104801 (2018).

Published under license by AIP Publishing

[25]G. La Forgia and G. Sciortino, "The role of the free surface on interfacial solitary waves," Phys. Fluids **31**, 106601 (2019).
[26]R. Amen and T. Maxworthy, "The gravitational collapse of a mixed region into a linearly stratified fluid," J. Fluid Mech. **96**, 65–80 (1980).
[27]R. E. Britter and J. E. Simpson, "A note on the structure of the head of an intrusive gravity current," J. Fluid Mech. **112**, 459–466 (1981).
[28]K. M. Faust and E. J. Plate, "Experimental investigation of intrusive gravity currents entering stably stratified fluids," J. Hydraul. Res. **22**, 315–325 (1984).
[29]F. De Rooij, P. F. Linden, and S. B. Dalziel, "Saline and particle-driven interfacial intrusions," J. Fluid Mech. **389**, 303–334 (1999).
[30]R. J. Lowe, P. F. Linden, and J. W. Rottman, "A laboratory study of the velocity structure in an intrusive gravity current," J. Fluid Mech. **456**, 33–48 (2002).
[31]B. R. Sutherland, "Interfacial gravity currents. I. Mixing and entrainment," Phys. Fluids **14**, 2244–2254 (2002).
[32]A. P. Mehta, B. R. Sutherland, and P. J. Kyba, "Interfacial gravity currents. II. Wave excitation," Phys. Fluids **14**, 3558–3569 (2002).
[33]B. R. Sutherland and J. T. Nault, "Intrusive gravity currents propagating along thin and thick interfaces," J. Fluid Mech. **586**, 109–118 (2007).
[34]H.-B. Cheong, J. J. P. Kuenen, and P. F. Linden, "The front speed of intrusive gravity currents," J. Fluid Mech. **552**, 1–11 (2006).
[35]M. R. Flynn and P. F. Linden, "Intrusive gravity currents," J. Fluid Mech. **568**, 193–202 (2006).
[36]G. la Forgia, L. Ottolenghi, C. Adduce, and F. Falcini, "Intrusions and solitons: Propagation and collision dynamics," Phys. Fluids **32**, 076605 (2020).
[37]C. Härtel, E. Meiburg, and F. Necker, "Analysis and direct numerical simulation of the flow at a gravity-current head. Part 1. Flow topology and front speed for slip and no-slip boundaries," J. Fluid Mech. **418**, 189–212 (2000).
[38]M. I. Cantero, J. R. Lee, S. Balachandar, and M. H. Garcia, "On the front velocity of gravity currents," J. Fluid Mech. **586**, 1–39 (2007).
[39]M. Cantero, S. Balachandar, M. García, and D. Bock, "Turbulent structures in planar gravity currents and their influence on the flow dynamics," J. Geophys. Res.: Oceans **113**, 1–22, https://doi.org/10.1029/2007jc004645 (2008).
[40]S. K. Ooi, G. Constantinescu, and L. Weber, "Numerical simulations of lock-exchange compositional gravity current," J. Fluid Mech. **635**, 361–388 (2009).
[41]T. Tokyay, G. Constantinescu, and E. Meiburg, "Lock-exchange gravity currents with a high volume of release propagating over a periodic array of obstacles," J. Fluid Mech. **672**, 570–605 (2011).
[42]L. Ottolenghi, C. Adduce, R. Inghilesi, F. Roman, and V. Armenio, "Mixing in lock-release gravity currents propagating up a slope," Phys. Fluids **28**, 056604 (2016).
[43]L. Ottolenghi, C. Adduce, F. Roman, and V. Armenio, "Analysis of the flow in gravity currents propagating up a slope," Ocean Modell. **115**, 1–13 (2017).
[44]S. Chawdhary, A. Khosronejad, G. Christodoulou, and F. Sotiropoulos, "Large eddy simulation of density current on sloping beds," Int. J. Heat Mass Transfer **120**, 1374–1385 (2018).
[45]S. K. Ooi, G. Constantinescu, and L. J. Weber, "2D large-eddy simulation of lock-exchange gravity current flows at high Grashof numbers," J. Hydraul. Eng. **133**, 1037–1047 (2007).
[46]M. A. Khodkar, M. Nasr-Azadani, and E. Meiburg, "Intrusive gravity currents propagating into two-layer stratified ambients: Vorticity modeling," Phys. Rev. Fluids **1**, 044302 (2016).
[47]S. B. Pope, *Turbulent Flows* (Cambridge University Press, 2000), pp. 558–586.
[48]V. Armenio and S. Sarkar, "An investigation of stably stratified turbulent channel flow using large-eddy simulation," J. Fluid Mech. **459**, 1–42 (2002).
[49]J. R. Taylor, S. Sarkar, and V. Armenio, "Large eddy simulation of stably stratified open channel flow," Phys. Fluids **17**, 116602 (2005).
[50]R. Inghilesi, C. Adduce, V. Lombardi, F. Roman, and V. Armenio, "Axisymmetric three-dimensional gravity currents generated by lock exchange," J. Fluid Mech. **851**, 507–544 (2018).
[51]C. Meneveau, T. S. Lund, and W. H. Cabot, "A Lagrangian dynamic subgrid-scale model of turbulence," J. Fluid Mech. **319**, 353–385 (1996).
[52]Y. Zang, R. L. Street, and J. R. Koseff, "A non-staggered grid, fractional step method for time-dependent incompressible Navier-Stokes equations in curvilinear coordinates," J. Comput. Phys. **114**, 18–33 (1994).
[53]V. Armenio and U. Piomelli, "A Lagrangian mixed subgrid-scale model in generalized coordinates," Flow, Turbul. Combust. **65**, 51–81 (2000).
[54]B. R. Sutherland, P. J. Kyba, and M. R. Flynn, "Intrusive gravity currents in two-layer fluids," J. Fluid Mech. **514**, 327–353 (2004).
[55]A. R. Osborne and T. L. Burch, "Internal solitons in the Andaman Sea," Science **208**, 451–460 (1980).

Published under license by AIP Publishing